

Lightning radio source retrieval using Advanced Lightning Direction Finder (ALDF) networks

W. J. Koshak and R. J. Blakeslee

Global Hydrology and Climate Center, NASA Marshall Space Flight Center,
Huntsville, Alabama

J. C. Bailey

Raytheon STX, Global Hydrology and Climate Center, NASA Marshall Space Flight
Center, Huntsville, Alabama

Abstract. A linear algebraic solution is provided for the problem of retrieving the location and time of occurrence of lightning ground strikes from an Advanced Lightning Direction Finder (ALDF) network. The ALDF network measures field strength, magnetic bearing, and arrival time of lightning radio emissions. Solutions for the plane (i.e., no Earth curvature) are provided that implement all of the measurements mentioned above. Tests of the retrieval method are provided using computer-simulated data sets. We also introduce a quadratic planar solution that is useful when only three arrival time measurements are available. The algebra of the quadratic root results are examined in detail to clarify what portions of the analysis region lead to fundamental ambiguities in source location. Complex root results are shown to be associated with the presence of measurement errors when the lightning source lies near an outer sensor baseline of the ALDF network. In the absence of measurement errors, quadratic root degeneracy (no source location ambiguity) is shown to exist exactly on the outer sensor baselines for arbitrary non-collinear network geometries. The accuracy of the quadratic planar method is tested with computer generated data sets. The results are generally better than those obtained from the three station linear planar method when bearing errors are about 2° . We also note some of the advantages and disadvantages of these methods over the nonlinear method of χ^2 minimization employed by the National Lightning Detection Network (NLDN) and discussed in Cummins et al. (1993, 1995, 1998).

1. Introduction

Advanced Lightning Direction Finder (ALDF) sensors developed by Global Atmospheric Inc. (GAI), have the ability to detect the field strength, magnetic bearing, and arrival time of lightning radio emissions. In 1992, Lightning Location and Protection, Inc. (a division of GAI) completed development of an IMproved PerformAnce from Combined Technology (IMPACT) method for determining the location and time of occurrence of lightning return strokes from these data [Cummins *et al.*, 1993]. The IMPACT algorithm is based on minimizing a χ^2 function similar to that provided in (1) of Hiscox *et al.* [1984] but generalized to accommodate arrival time data. A primary advantage of the IMPACT method is that it accounts for the effects of Earth curvature. However, since the algorithm is a *nonlinear* iterative approach it does not represent an *analytic* solution to the problem, i.e., the source location and time of occurrence are not directly determined in terms of the measurements and measuring network geometry.

In the current study, we go back and carefully reexamine various forms of the retrieval problem cited above for planar geometries, i.e., neglecting Earth curvature. Our intent is not necessarily to improve upon results obtained from the IMPACT method, but rather to lay down a detailed formalism for solving the retrieval problem when Earth curvature is neglected. We are motivated by a desire to specifically determine the source location (x, y) as a mathematical function of the measurements under of variety of conditions (i.e., differences in the number, location, and type of measurements). Since algebraic solutions are obtained, we do not need to invoke a computer search algorithm to determine optimum solution parameters. The accuracy of search algorithms (e.g., χ^2 minimization) depend, in general, on search parameter initialization, and on the presence of multiple minima. Finally, we feel that more physical insight into the nature of the retrieval problem is obtained by determining how the measurements are specifically related to the lightning source location (and time of occurrence).

A Linear Planar (LP) method is first introduced that allows one to *simultaneously* analyze field, bearing, and arrival time measurements. The method involves one large system of linear

equations that offers a high degree of flexibility from the point-of-view of the user's applicational needs. For example, if only a certain number and type of measurements are available in an experiment, the linear system of equations degenerates into a smaller set of equations, and a straight-forward solution process is retained.

We also introduce a Quadratic Planar (QP) method that can be used when only three arrival time measurements are available. Such a situation arises if there are sensor hardware failures and/or when field amplitude and bearing measurement data quality is unacceptable. Although this method is mathematically nonlinear, full analytic solutions are derived. Physical insight about the nonlinear solution space, not discernible from conventional χ^2 analyses, is fully described by examining in detail all quadratic root solutions derived from the QP method.

Extensive tests of the LP and QP retrieval methods are provided using computer-simulated data sets because these methods will be applied in a future study of ALDF data that were obtained during the Maritime Continent Thunderstorm EXperiment (MCTEX) in Darwin, Australia [Kennen *et al.*, 1994; 1996]. Data from this network comprise one of several ground-truth sites for the validation of NASA's space-based lightning detectors (the Lightning Imaging Sensor (LIS) and the Optical Transient Detector (OTD) described in Christian *et al.* [1992] and Goodman *et al.* [1995], respectively).

2. Linear Planar (LP) Method

We begin by considering $n \geq 3$ sensors situated at locations \mathbf{r}_i , $i = 1, 2, \dots, n$ relative to some origin. Each sensor has the capability to measure the arrival time, t_i , magnetic bearing, ϕ_i , and field strength, F_i , of the radio emissions from a lightning source with location, \mathbf{r} , time of occurrence, t , and radiation source strength, s . Hence, from the $3n$ measurements $\{(t_1, \phi_1, F_1), \dots, (t_n, \phi_n, F_n)\}$ we wish to determine the five unknowns (\mathbf{r}, t, s) . In so doing, we neglect Earth curvature.

Figure 1 summarizes the geometry of the LP model. Because ALDF sensors might not be deployed on a flat topography, the i^{th} sensor located at \mathbf{r}_i need not lie in the xy plane, i.e., $z_i \neq 0$ in

general. The relative position vector follows standard physics convention, that is, it points from the source at \mathbf{r} to the observation point, \mathbf{r}_i , so that $\mathbf{R}_i = \mathbf{r}_i - \mathbf{r}$. Neglecting refractive effects in the atmosphere, the excitation time of the i^{th} sensor is

$$t_i = t + \frac{1}{c} R_i, \quad (1)$$

where c is the speed of light. Solving for R_i , squaring, and rearranging terms leads to

$$\frac{1}{2}(r_i^2 - c^2 t_i^2) = x_i x + y_i y + z_i z - c^2 t_i t - \frac{1}{2}(r^2 - c^2 t^2). \quad (2)$$

It is desirable to remove the last term on the right-hand side of (2) since it is nonlinear in the space and time variables. To do this, we define the measurement

$$\alpha_i \equiv \frac{1}{2}(r_i^2 - c^2 t_i^2) - \frac{1}{2}(r_1^2 - c^2 t_1^2). \quad (3)$$

A comparison of (2) and (3) shows that α_i is linearly related to the lightning location, $\mathbf{r} = (x, y, z)$, and lightning time of occurrence, t , that is,

$$\alpha_i = (x_i - x_1)x + (y_i - y_1)y + (z_i - z_1)z - c^2(t_i - t_1)t; \quad i = 2, 3, \dots, n. \quad (4)$$

A detailed investigation of this linear form has been provided in *Koshak and Solakiewicz [1996]*.

Next, we consider the information content of ALDF bearing data. From Figure 1 we see that the lightning location (x, y) is given by

$$x = x_i + \rho_i \cos \phi_i \quad (5)$$

$$y = y_i + \rho_i \sin \phi_i .$$

It is useful to define the measurement

$$\beta_i \equiv x_i \sin \phi_i - y_i \cos \phi_i . \quad (6)$$

Now from (5) we note that $(x - x_i)/(y - y_i) = \cos \phi_i / \sin \phi_i$, so that using (6) gives

$$\beta_i = \sin \phi_i x - \cos \phi_i y . \quad (7)$$

Finally, we consider measurements of the radiated field strength. Assuming a $1/R_i$ attenuation in the radiation field gives

$$F_i = \frac{1}{R_i} s . \quad (8)$$

Once again, we solve for R_i , square, rearrange terms, and define the measurement

$$\gamma_i \equiv \frac{1}{2}(r_i^2 - r_1^2) . \quad (9)$$

This leads to the following relation

$$\gamma_i = (x_i - x_1)x + (y_i - y_1)y + (z_i - z_1)z + \frac{1}{2} \left(\frac{1}{s_i^2} - \frac{1}{s_1^2} \right) s^2 ; \quad i = 2, 3, \dots, n . \quad (10)$$

If we consider only $n = 3$ sensors, (4), (7), and (10) can be combined to give

$$\begin{bmatrix} \alpha_2 \\ \alpha_3 \\ \delta\beta_1 \\ \delta\beta_2 \\ \delta\beta_3 \\ \gamma_2 \\ \gamma_3 \end{bmatrix} = \begin{bmatrix} (x_2 - x_1) & (y_2 - y_1) & (z_2 - z_1) & c(t_1 - t_2) & 0 \\ (x_3 - x_1) & (y_3 - y_1) & (z_3 - z_1) & c(t_1 - t_3) & 0 \\ \delta \sin \phi_1 & -\delta \cos \phi_1 & 0 & 0 & 0 \\ \delta \sin \phi_2 & -\delta \cos \phi_2 & 0 & 0 & 0 \\ \delta \sin \phi_3 & -\delta \cos \phi_3 & 0 & 0 & 0 \\ (x_2 - x_1) & (y_2 - y_1) & (z_2 - z_1) & 0 & \psi_2(x_2 - x_1) \\ (x_3 - x_1) & (y_3 - y_1) & (z_3 - z_1) & 0 & \psi_3(x_2 - x_1) \end{bmatrix} \begin{bmatrix} x \\ y \\ z \\ d_t \\ d_s \end{bmatrix}, \quad (11)$$

where δ is a weighting factor chosen as 10^3 meters, $\psi_i = \frac{1}{2}[(F_1/F_i)^2 - 1]$ is a dimensionless parameter, $d_t = ct$, $d_s = \xi^2 s^2$, and $\xi = [F_1(x_2 - x_1)^{1/2}]^{-1}$ is a scaling factor to be described below. Defining the column vector on the left-hand side of (11) as \mathbf{g} , the matrix by \mathbf{K} , and the remaining vector by \mathbf{f} , we may rewrite (11) as

$$\mathbf{g} = \mathbf{K}\mathbf{f}. \quad (12)$$

All elements of \mathbf{K} and \mathbf{f} are in units of meters, and all elements of \mathbf{g} are in squared meters. This was accomplished by retaining a factor of c in front of the time difference measurements in the first two rows (fourth column) of \mathbf{K} , by multiplying (7) by the weighting factor δ , and by scaling the field, F_i , and source strength, s , each by the factor ξ , i.e., by making the substitutions: $F_i \rightarrow \xi F_i$, and $s \rightarrow \xi s$ in (8). [Note that the sites must be numbered in such a way that $x_2 > x_1$ so ξ is not complex; this can always be accomplished since the numbering of sites is arbitrary and because the translation and rotation of the xy coordinate system used in the LP method is arbitrary.]

In general, the \mathbf{K} matrix has $3n-2$ rows and 5 columns, where $n = 1, 2, 3, \dots$. If there is only $n = 1$ sensors in the network, \mathbf{K} degenerates into a row vector and (12) is underdetermined. If there are $n = 2$ sensors, \mathbf{K} will have 4 rows and (12) will still be underdetermined. For $n \geq 3$ sites,

\mathbf{K} will have ≥ 7 rows and (12) will be overdetermined. For overdetermined systems, \mathbf{f} can be retrieved using the least-squares inversion provided in *Twomey* [1977]

$$\mathbf{f} = (\tilde{\mathbf{K}}\mathbf{K})^{-1} \tilde{\mathbf{K}}\mathbf{g} \quad , \quad (13)$$

where the tilde represents matrix transposition. The source time of occurrence and source strength are determined as: $t = d_t / c$, $s = d_s^{1/2} / \xi$, respectively.

From the foregoing generalities, we now note that ALDF sensors are intended to trigger only on the ground wave of a cloud-to-ground discharge. Hence, the source can be regarded as being located at $z = 0$. In this case, we can remove the third component of \mathbf{f} , that is, we consider the column vector $\mathbf{f} \equiv \text{col}(x, y, d_t, d_s)$, and we remove the third column of \mathbf{K} . We then regard the expression in (12) as a $(3n-2)$ by 4 system of linear equations. In this case, $n = 2$ sensors generates a (4×4) \mathbf{K} matrix so that (12) is a determined system with direct solution $\mathbf{f} = \mathbf{K}^{-1}\mathbf{g}$. Hence, the LP method can be used by an experimenter that has only two sensors, each measuring bearing, arrival time, and field amplitude. In this case, source location (x,y) , time of occurrence, t , and source strength, s , can be retrieved. If the two sensors do not provide field amplitude information, the experimenter can still retrieve the flash location and time of occurrence, i.e., (12) becomes a (3×3) system of linear equations, and $\mathbf{f} = \text{col}(x,y,d_t)$.

If δ is unity, the row vectors of \mathbf{K} involving $\sin\phi_i$ and $\cos\phi_i$ appear numerically small i.e., like a zero vector, relative to the other row vectors of \mathbf{K} , and the matrix is ill-conditioned for many source locations when only three ALDF sensors are available.

To avoid unstable inversions associated with an ill-conditioned \mathbf{K} -matrix, we have made the assignment $\delta = 10^3$ meters. This increases the magnitude of the small trigonometric components of \mathbf{K} and effectively filters small eigenvalues; see section 3.4 below and Appendix A for additional details regarding the value of δ . Other, more sophisticated means of filtering small

eigenvalues by adding external physical constraints to the solution process are discussed in Twomey [1977], Chapter 6.

3. Simulated Tests of the LP Method

3.1 Overview

In this and all tests to follow, we do not consider the field amplitude data, F_i . We also assume that all sources and sensors are located on the surface of a spherical Earth. By selecting a known source latitude/longitude location, we generate the true arrival times and bearings to each sensor. Simulated measurements are generated by adding errors to the computed arrival times and bearings. The errors are chosen from a uniform random distribution.

Next, the simulated measurements are analyzed with the LP method. Since the LP method is a planar model, we must establish a convention for mapping source and sensor locations (expressed in degrees of latitude and longitude) to locations in the xy -plane of a standard Cartesian coordinate system. We then apply the LP method to solve the problem in the Cartesian system. Next, an inverse mapping is used to convert the (x, y) solution back into latitude and longitude coordinates on the surface of the Earth. At this point, the latitude/longitude solution can be compared with the known source to assess true location error.

If one assumes a flat Earth and performs the entire simulation within a Cartesian coordinate system, the resulting retrieval errors are smaller. This is because one avoids errors due to Earth curvature and the numerical errors associated with spherical/Cartesian system mappings. Because in any real field experiment the source retrievals are ultimately referenced to the spherical Earth, we include the net effects of Earth sphericity in this and all other simulations provided below.

3.2 Spherical Arrival Time and Bearing

Figure 2 indicates how to compute the arrival time, t_i , and bearing, ϕ_i , for the i^{th} sensor on a sphere. The unit vectors pointing from the origin O : to the i^{th} sensor (M), to the lightning source (L), and to the North Pole (N) are, respectively,

$$\begin{aligned}
\hat{\mathbf{r}}_i &= \cos \varphi_i \cos \lambda_i \hat{\mathbf{u}} + \cos \varphi_i \sin \lambda_i \hat{\mathbf{v}} + \sin \varphi_i \hat{\mathbf{w}} \\
\hat{\mathbf{r}} &= \cos \varphi \cos \lambda \hat{\mathbf{u}} + \cos \varphi \sin \lambda \hat{\mathbf{v}} + \sin \varphi \hat{\mathbf{w}} \\
\hat{\mathbf{r}}_N &= \hat{\mathbf{w}} .
\end{aligned} \tag{14}$$

Using the law of cosines from spherical trigonometry gives the spherical angle, A_i :

$$A_i = \frac{180}{\pi} \cos^{-1} \left(\frac{\cos a - \cos b_i \cos c_i}{\sin b_i \sin c_i} \right) , \tag{15}$$

where $a = \cos^{-1}(\hat{\mathbf{r}}_N \cdot \hat{\mathbf{r}})$, $b_i = \cos^{-1}(\hat{\mathbf{r}}_N \cdot \hat{\mathbf{r}}_i)$, $c_i = \cos^{-1}(\hat{\mathbf{r}}_i \cdot \hat{\mathbf{r}}) = \frac{1}{R} ct_i$, R = radius of Earth, and by convention the lightning source activates at $t \equiv 0$. The angle, A_i , varies between 0° (North) and 180° (South). We correct A_i to construct the bearing function, ϕ_i , that varies in the manner: 0° (East), 90° (North), 180° (West), 270° (South), that is,

$$\begin{aligned}
\phi_i &= 90 - A_i \quad (\text{North East sources}) \\
\phi_i &= 90 + A_i \quad (\text{North West \& South West sources}) \\
\phi_i &= 450 - A_i \quad (\text{South East sources}) .
\end{aligned} \tag{16}$$

3.3 Mappings

In general, different mappings produce different retrieval errors. We consider two possible approaches: Mapping #1 (chosen for its mathematical simplicity), and Mapping #2 (chosen for its orthogonality). In Mapping #1, we have

$$\begin{aligned}
 x &= (\lambda - \lambda_1) R \cos \varphi_1 \\
 y &= (\varphi - \varphi_1) R \quad ,
 \end{aligned}
 \tag{17}$$

where (λ, φ) is an arbitrary longitude and latitude, respectively. The origin of the Cartesian coordinate system has been arbitrarily selected as site $i = 1$, i.e., the ordered pair (λ_1, φ_1) is the location of site 1 and $x(\lambda = \lambda_1, \varphi = \varphi_1) = 0$, $y(\lambda = \lambda_1, \varphi = \varphi_1) = 0$. Note that y is measured along a great circle, i.e., a longitude belt, but that x is measured along a latitude belt [which is only a great circle if $\varphi_1 = 0$ (the Equator)].

In the second approach, or Mapping #2, we insist that both x and y are measured along great circles. To do this, we consider an orthogonal system $(\hat{\mathbf{u}}, \hat{\mathbf{v}}, \hat{\mathbf{w}})$ where $\hat{\mathbf{u}}$ is a unit vector directed from the center of the Earth to the intersection of the Prime Meridian and Equator, $\hat{\mathbf{w}}$ is a unit vector directed from the center of the Earth to the North Pole, and $\hat{\mathbf{v}}$ completes the ordered triple in accordance with the right-hand rule, i.e., $\hat{\mathbf{v}} \equiv \hat{\mathbf{w}} \times \hat{\mathbf{u}}$. We then rotate this coordinate system through two Euler angles (λ_1, φ_1) and define the new resultant ("starred") system as $(\hat{\mathbf{u}}^*, \hat{\mathbf{v}}^*, \hat{\mathbf{w}}^*)$. In the starred system, $\hat{\mathbf{u}}^*$ is directed from the center of the Earth to site 1. Mapping #2 is then

$$\begin{aligned}
 x &= R \lambda^*(\lambda, \varphi) \\
 y &= R \varphi^*(\lambda, \varphi) \quad ,
 \end{aligned}
 \tag{18}$$

where

$$\begin{aligned}
 \lambda^*(\lambda, \varphi) &= \tan^{-1} \left(\frac{\cos \varphi \sin \lambda \cos \lambda_1 - \cos \varphi \cos \lambda \sin \lambda_1}{\cos \varphi \cos \lambda \cos \lambda_1 \cos \varphi_1 + \cos \varphi \sin \lambda \sin \lambda_1 \cos \varphi_1 + \sin \varphi \sin \varphi_1} \right) \\
 \varphi^*(\lambda, \varphi) &= \sin^{-1} \left(\sin \varphi \cos \varphi_1 - \cos \varphi \cos \lambda \cos \lambda_1 \sin \varphi_1 - \cos \varphi \sin \lambda \sin \lambda_1 \sin \varphi_1 \right) .
 \end{aligned}
 \tag{19}$$

Again, one can verify from (18) and (19) that $x(\lambda = \lambda_1, \varphi = \varphi_1) = 0$, $y(\lambda = \lambda_1, \varphi = \varphi_1) = 0$. The arctangent expression in (19) must be appropriately corrected depending on what quadrant (North East, North West, South East, South West) the point (λ, φ) is relative to site 1.

3.4 Simulation

We first consider three ALDF sites in the Darwin, Australia region that were used as part of the MCTEX described in *Keenan et al.* [1994; 1996]. Computer-generated lightning sources were spaced 0.02° (~ 2 km) apart across the analysis region. Figure 3a shows the spatial distribution of the retrieved horizontal source location error, contoured in units of kilometers, when no experimental errors are considered and when Mapping #1 is used. The retrieved location errors are within 1 km for regions outside the ALDF network.

Since no experimental errors have been added to the simulated values of the arrival times and bearings, the retrieval errors shown in Figure 3a are due solely to Earth curvature and numerical truncation error. We originally performed these simulations, and all simulations to follow, assuming a flat Earth. When this was done, all of our methods gave retrieval errors well below 2.5 meters across the entire analysis region when no measurement errors were involved. This is to be expected since our methods are exact solutions for the plane (the 2.5 meter error maximum occurred only in the LP method over a limited portion of the analysis region and was an artifact of what accuracy level we required of our iterative matrix inversion routine). Hence, compared to the negligible errors obtained from the flat Earth simulations, the errors shown in Figure 3a are effectively due to Earth curvature alone. However, the amount of retrieval error due to Earth curvature depends on what cartesian-to-spherical coordinate system mapping is used (e.g., Mapping #1, or Mapping #2). Because one will always be interested in how much retrieval error the planar models acquire due to Earth curvature, all simulations below show retrievals first without added measurement errors, as in Figure 3a.

When experimental errors are included in the simulation, we obtain the retrieved location errors given in Figure 3b. The retrieved errors are mean values obtained from performing 100

individual retrievals at each trial location. For each of the 100 trials, an arrival time error selected from a uniform random distribution (ranging from -300 ns to 300 ns) is added to the arrival time value, and a bearing error (ranging from -2° to 2°) is added to the bearing value. In addition, we have simulated sensor location errors by purposely entering into the LP method false site locations (with an error as great as one-half meter); the sensor location errors have remained fixed for all source analyses. As expected, the addition of experimental errors increases location retrieval errors, but the retrieved errors are still within 10 km for a large portion of the analysis region. Roughly speaking, i.e., not accounting for Earth curvature errors, truncation errors, or other errors due to matrix inversion, a 300 ns timing error multiplied by the speed of light gives only a 90 meter error, and a 2° error at a range of 300 km is about 10 km.

When Mapping #2 is used instead of Mapping #1, we obtain the results shown in Figures 4a and 4b. As before, no experimental errors have been added to the sensor positions, arrival times, and bearings in the results of Figure 4a, but the results in Figure 4b include these errors. The results in Figure 4a appear somewhat better than those in Figure 3a, but the results in Figures 3b and 4b are similar.

Figures 5a, 5b, 6a, and 6b show all of the same type of analyses just described, but for the case of four ALDF sensors. The additional sensor clearly helps reduce retrieval error. In addition, Mapping #2 produces smaller retrieval errors than Mapping #1.

When four sensors are available, bearing data are not needed to obtain lightning location retrievals (see (11)). By removing the bearing data from the four-station MCTEX region simulations, that is assigning $\delta = 0$, and by applying Mapping #2 we obtained virtually the same results as those presented in Figures 6a and 6b. This is because the weighting factor δ introduced into (11) to generate Figures 6a and 6b is relatively small (i.e., 10^3) so that bearing data has little influence on the final solution. We also find little change in the solutions for intermediate values, $\delta = 10$, 10^2 . However, as we increase δ from 10^3 to 10^4 , 10^5 , and 10^6 the retrieval errors increase (see Appendix A for more details).

For a three sensor ALDF network, bearing data plays a more profound role in helping to constrain the solution space. If $\delta = 0$ (no bearing data used), there would be fewer constraint equations than unknowns, and one would not be able to obtain a solution using the LP formalism. [Note: a different formalism to be described in section 4 below can be used to find solutions over a substantial portion of the analysis region using just 3 arrival time sensors.] As noted above, when $\delta = 1$ the \mathbf{K} matrix is ill-conditioned for many source locations, and the computer time required to invert \mathbf{K} is excessive. When $\delta = 10, 10^2, 10^3$, or 10^4 there is no problem inverting \mathbf{K} and there is no appreciable change in retrieval error. When $\delta = 10^5$ the retrieval errors begin to increase slightly. Three station LP simulations for different values of δ are also provided in Appendix A.

For comparison, we also provide error results (Figs. 7a, 7b) for the three sites used in the Tropical Ocean Global Atmosphere Coupled Ocean-Atmosphere Response Experiment (TOGA COARE) described in *Orville et al. [1997]* and *Peterson et al. [1986]*. This experiment employed a larger sensor baseline than that used in MCTEX, and our simulated tests cover an analysis region $18^\circ \times 18^\circ$ in latitude and longitude. The sources in this simulation were placed 0.05° apart and Mapping #2 was used; as with the three sensor MCTEX study, the retrieval errors for Mapping #2 differ little from those errors obtained using Mapping #1. Overall, the 2° bearing error and the effects of Earth curvature make it difficult to obtain errors below 10 km for distant sources.

4. Quadratic Planar (QP) Method

In this section we assume that only three arrival time measurements are available from the ALDF network. Hence, the methods of section 2 cannot be applied, but some insight about the source location can still be obtained. Once again, considering only the radio emission from the lowest part of the return stroke, we take $z = 0$. We assume that sensor $i = 1$ is at the origin of a rectangular Cartesian coordinate system, i.e., $x_1 = y_1 = z_1 = 0$, and we specify the convention $t_1 \equiv 0$. This leads to one nonlinear equation and two linear equations all in the three unknowns (x, y, r)

$$x^2 + y^2 = r^2 \quad (20)$$

$$q'_i \equiv \frac{1}{2}(r_i^2 - c^2 t_i^2) = x_i x + y_i y + c t_i r ; \quad i = 2, 3 .$$

The equations in (20) were derived from the transit equation in (1) by means similar to that discussed prior to (2) of section 2. We have removed the source activation time, t , with the relation $t = -r/c$. Since $t_1 \equiv 0$, it is consistent that $t \leq 0$ given that $r \geq 0$. Each sensor is a distance $r_i = (x_i^2 + y_i^2)^{1/2}$ from the origin.

Fundamentally, these equations define three circles each with radius $c(t_i - t)$ and centers at (x_i, y_i) , where $i = 1, 2, 3$. We will see below that the source is located where the three circles intersect. We will also find that certain source locations produce arrival time data that can be described geometrically by *two* possible sets of three circles. Each set of three circles define a unique intersection point in the xy -plane thereby leading to a fundamental ambiguity in source location retrieval.

Geometric intersections of the circular curves described above are obtained by solving the system of equations in (20). To solve the system, we first subtract the terms $c t_i r$ from each side of the linear equation set

$$q_{i-1} \equiv q'_i - c t_i r = x_i x + y_i y ; \quad i = 2, 3 . \quad (21)$$

Identifying the vectors, $\mathbf{q} = \text{col}(q_1, q_2)$, $\mathbf{r} = \text{col}(x, y)$, we may write

$$\mathbf{q} = \mathbf{Q} \mathbf{r} , \quad (22)$$

where the \mathbf{Q} -matrix and it's inverse are given by

$$\mathbf{Q} = \begin{bmatrix} x_2 & y_2 \\ x_3 & y_3 \end{bmatrix}, \quad \mathbf{Q}^{-1} = \frac{1}{x_2 y_3 - y_2 x_3} \begin{bmatrix} y_3 & -y_2 \\ -x_3 & x_2 \end{bmatrix}. \quad (23)$$

From (22) and (23) and our discussion preceding (21) we have the relations

$$\begin{aligned} x(r) &= (y_3 q_1 - y_2 q_2) / (x_2 y_3 - y_2 x_3) \\ y(r) &= (x_2 q_2 - x_3 q_1) / (x_2 y_3 - y_2 x_3) \\ t(r) &= -r / c. \end{aligned} \quad (24)$$

The x and y variables are written as functions of r in (24) since the components of \mathbf{q} depend on r as given in (21). Substituting the first two equations of (24) into the first (nonlinear) equation of (20) and carrying out the algebra leads to an equation quadratic in r alone

$$Ar^2 + Br + C = 0, \quad (25)$$

where

$$\begin{aligned} A &= c^2 \left[r_3^2 t_2^2 - 2(x_2 x_3 + y_2 y_3) t_2 t_3 + r_2^2 t_3^2 \right] - (x_2 y_3 - y_2 x_3)^2 \\ B &= 2c \left[-r_3^2 q_2' t_2 + (x_2 x_3 + y_2 y_3) (q_2' t_3 + q_3' t_2) - r_2^2 q_3' t_3 \right] \\ C &= r_3^2 q_2'^2 - 2(x_2 x_3 + y_2 y_3) q_2' q_3' + r_2^2 q_3'^2. \end{aligned} \quad (26)$$

Hence, the lightning source range, r , is the *nonnegative real* root obtained from the formal (two root) solution

$$r = \begin{cases} r_+ = \frac{-B + \sqrt{B^2 - 4AC}}{2A} \\ r_- = \frac{-B - \sqrt{B^2 - 4AC}}{2A} \end{cases} \quad (27)$$

Values of $r = 0$ correspond to a direct lightning strike of sensor $i = 1$, which we ignore. Note from (26) that the numerical value of the coefficients (A , B , C) are obtained from the sensor locations and excitation times, that is, on the six variables: $\{x_2, y_2, t_2, x_3, y_3, t_3\}$; the variables, q'_i , are obtained from the expressions $\frac{1}{2}(r_i^2 - c^2 t_i^2)$ as given in the last two equations of (20). After these data are used to compute r , (24) is used to find the lightning location $(x(r), y(r))$, and time of occurrence, $t(r)$.

5. Simulated Tests of the QP Method

By placing computer-generated lightning sources 0.02° apart in latitude and longitude across the analysis area (see section 3), we have determined the horizontal location error resulting from each root in (27). To facilitate comparisons with simulated tests of the LP method, sensor position and arrival time errors used here are as described in section 3.4 and 100 trials at each source location are once again used to generate mean retrieval location errors. Mapping #1 given in (17) is employed.

Figure 8 clarifies what root provides a smaller retrieval error. The shaded regions are where r_+ provides a better retrieval than r_- (the unshaded region is where r_- provides a better retrieval than r_+). Interestingly, the dividing lines of these regions are defined by the sensor baselines.

When we pick only the root that provides the best retrieval and plot the associated error result over the analysis region, we obtain the result given in Figure 9a. When a 300-ns uniform

random error is added to the computer-generated arrival times, we obtain the mean horizontal distance errors given in Figure 9b. Considering that only three sensors are involved, retrieval errors are quite good; a large region of errors below 1 km is evident. Distant sources, or sources located near the outer sensor baselines are more difficult to accurately retrieve. By *outer sensor baseline* we mean: any position along a great circle passing through 2 sensors except those points on the great circle located between the two sensors. A comparison between the three station LP results in Figure 3b shows that the QP method provides better results over most of the analysis region. This is due in part to the large 2° bearing errors implemented in the LP simulation and the fact that the three station LP method depends on bearing data to obtain a solution. The four station LP method (Figure 5b) outperforms the QP method.

Since bearing data can aid in determining which root, r_+ or r_- , is correct (see section 6.1 below on solution ambiguity) and since the QP method gives generally better results than the 3 sensor LP method, it is evidently better to use the QP method than the 3 station LP method even when bearing data are available. This conclusion is based, of course, on an assumed bearing error of 2° .

6. Examination of QP Method Roots

When applying the QP method to actual arrival time data, one picks the solution associated with a nonnegative real root, i.e., the source range, r , must be nonnegative and real. A detailed discussion of root results is provided below.

6.1 Unequal Nonnegative Real Roots (Ambiguities)

In the discussion of three sensor networks by *Holle and Lopez* [1993], pp. 8 and 11, the lightning source location (x, y) is described in terms of the intersection of two hyperbola branches; each branch is defined by two sensors. For some lightning source locations, the hyperbola branches intersect at *two* locations [see for instance, Fig. 6, p. 11 of *Holle and Lopez*, 1993]. This amounts to a fundamental ambiguity in location retrieval and the authors correctly assert that

the ambiguity can be removed by adding a fourth (properly positioned) sensor. Ambiguities are described in our formalism by the intersection of circles as indicated above following (20). To fully appreciate the hyperbolic and circular geometrical viewpoints, it is important to recognize that the two intersection points defined by two sets of three circles are identical to the double intersections obtained from the two hyperbola branches mentioned above. In other words, these two widely different geometrical viewpoints produce identical results, as they must.

Without reference to the geometry of hyperbolic or circular intersections, our algebraic formalism immediately defines all ambiguous cases. An ambiguity will exist whenever two unequal nonnegative real roots result from (27). In order to determine what lightning source locations produce these “ambiguity regions”, we have kept a record of the root results in the numerical experiments described in section 5 above. For the case of no simulated experimental errors, the source locations that resulted in two unequal nonnegative real roots are indicated by the shaded regions in Figure 10; see section 6.2 below for minor corrections to the ambiguity regions. In general, a different network geometry would produce different results.

Strictly speaking, since two distinct sources can produce identical arrival time difference information, there is no means of discriminating which source location is correct unless some additional information is supplied to the retrieval process. In effect, the solution is fundamentally nonunique. [Similar comments about the retrieval of charge from ground-based field measurements have been made in *Koshak and Krider* [1994]. In that problem, a point charge Q_o , and a sphere of radius a with total charge Q_o produce identical electrostatic fields outside the radius a .] Hence, additional measurements (e.g., arrival time, bearing, signal amplitude, radar, acoustical, interferometric) must be used to pick the correct root. Bearing data would be the most common data to use in root discrimination since it is part of the ALDF data stream.

Nonetheless, an experimenter might be tempted to compare the shaded regions in Figures 8 and 10 in order to determine which of the two unequal nonnegative real roots produce the true source location. However, one must remember that Figure 8 does not pose a real physical

constraint to an unknown source since it *only provides information if the source location is already known*; obviously in a real field experiment the source location is not yet known.

Additional rigor clarifies the immutability of the ambiguous case. Note that there are three ambiguity regions in Figure 10, and call the regions $\{R_1, R_2, R_3\}$. Similarly, there are three regions $\{P_1, P_2, P_3\}$ in Figure 8 that are wholly contained within each of the respective ambiguity regions. If one subtracts the respective regions $\{P_1, P_2, P_3\}$ from the respective regions $\{R_1, R_2, R_3\}$, one obtains the three regions $\{N_1, N_2, N_3\} \equiv \{R_1 - P_1, R_2 - P_2, R_3 - P_3\}$. When two unequal nonnegative real roots are obtained, we find that r_+ occurs in P_i and r_- occurs in N_i , that is, the pair of roots produce solutions in (P_1, N_1) , (P_2, N_2) , or (P_3, N_3) . From Figure 8, region P_i is the region where r_+ is correct, N_i is the region where r_- is correct, and both P_i and N_i are subregions of R_i . In other words, each solution is possibly correct so that comparisons between Figure 8 and Figure 10 serve no help in determining the correct root.

Nonetheless, r_+ is correct for most of the ambiguity region shown in Figure 10. Hence, an experimenter who obtains two nonnegative real roots, but who does not have ancillary data sets such as radar, magnetic bearing, etc., has a better chances of getting the correct solution if he/she selects the root r_+ .

6.2 Equal Nonnegative Real Roots

In this section we are interested in identifying what source locations produce two *equal* nonnegative real roots. Note that this condition is satisfied when the discriminant, $B^2 - 4AC$, in (27) is zero, that is, the two equivalent roots correspond to a unique (unambiguous) solution $[x(r), y(r), t(r)]$ where $r_+ = r_- = r$. In Appendix B, we show for arbitrary non-collinear network geometries that the discriminant function is zero *only along the outer sensor baselines*. Therefore, the ambiguity regions shown in Figure 10 are technically not ambiguous along these linear domains.

6.3 Complex Roots

Complex roots occur whenever the discriminant in (27) becomes negative. Figure 11 shows how the discriminant varies for different source locations across the analysis region. As we have already shown in section 6.2 and Appendix B, the discriminant is zero for sources located along the outer sensor baselines. Figure 11 shows additionally that the discriminant is a relative minimum at the outer sensor baselines.

From the simulation in section 5 (with 300-ns arrival time errors, and 100 trials per test location) we have tallied the fraction of trials at each location that produce complex roots. Figure 12 shows that there are no complex roots over most of the analysis region except when the sources are near the outer sensor baselines. These regions (or “spokes”) appear to diverge with range from the sensors and as many as 40–60% of the sources are complex within the spokes. Clearly, for sources located sufficiently close to the outer sensor baselines, measurement errors are occasionally large enough to drive the discriminant negative. Whenever the discriminant is negative, both roots in (27) are complex and no physical solution is obtained. Conversely, whenever complex roots are obtained from a set of actual measurements the source is likely to be located in one of the spoked regions.

6.4 Overview of Root Results

From our discussion so far, we can conclude that any retrieval will produce one of the following cases: (a) $r_+ \geq 0$, $r_- \geq 0$, $r_+ \neq r_-$; (b) $r_+ \geq 0$, $r_- \geq 0$, $r_+ = r_-$; (c) $r_+ < 0$, $r_- \geq 0$; or (d) r_+ and r_- complex. Case (a) corresponds to a source that is located inside one of the ambiguity regions, case (b) corresponds to a source located on an outer sensor baseline, case (c) corresponds to a source that is not located in any of the ambiguity regions or along any outer sensor baseline, and case (d) corresponds to a source located on or near any outer sensor baseline when measurement errors are sufficient to drive the discriminant negative.

Note that we do not include the case $r_+ \geq 0$, $r_- < 0$ since if $r_+ \geq 0$, the source must lie in one of the ambiguity regions implying that r_- would be nonnegative (i.e., a contradiction). We also

disregard the case that both roots are negative since a physical source must lie a nonnegative distance from sensor $i = 1$.

7. Summary

In this writing we have introduced two methods for retrieving the location and time of occurrence of lightning sources from a network of ALDF sensors. The first approach, or LP method, assumes that arrival time, bearing, and field amplitude measurements are all available from the network. As provided in (12), these measurements are collected into one coherent linear system of equations that is solved by straightforward inversion. Because of the general form of (12), we have clarified what solution options one has if only a subset of the measurements are available and/or if one or more sensors could not trigger on an event. In the extreme case of having only three arrival time measurements from the ALDF network (as might be the case due to sensor subsystem failure), we have introduced the QP method.

Perhaps the most compelling reason for working with the above methods is that each represent an algebraic solution. The planar methods express the source locations directly in terms of the measurements. The solutions are concise, require little computer time, and afford the user with specific physical insights about the retrieval problem (e.g., relative importance/effects of timing/bearing data on final solution, regions of ambiguity, source locations producing complex roots). This starkly contrasts the approach of nonlinear χ^2 minimization discussed in *Cummins et al.* (1993, 1995, 1998) and *Hiscox et al.* (1984) wherein solutions are found by a *computer search* of the optimum lightning source parameters (latitude, longitude, and time of occurrence). Solutions derived from χ^2 minimization techniques depend, in general, on what starting values are chosen for the lightning source parameters and solution errors arise due to the presence of relative multiple minima in the χ^2 surface. Nonetheless, the nonlinear minimization approach does account for Earth curvature and the extra computational time imposed by the method has not posed any practical problems owing to the exceptional speed of modern digital computers.

If in the future more sensors are added to the National Lightning Detection Network (NLDN) the average sensor baseline will decrease, and the range between a lightning source and the four nearest sensors will decrease. Consequently, the adverse effects of Earth curvature are reduced as more sensors are added, and the planar methods provided here become more attractive.

Moreover, the LP and QP methods introduced here offer the authors and other researchers at the NASA-Marshall Space Flight Center (MSFC) a means to intensively analyze and compare, first hand, lightning radio source locations in the MCTEX analysis region with OTD/LIS low Earth orbit lightning detections.

In the future, we intend to apply the methods to analyze a wide range of thunderstorms, to intercompare the methods, and to relate the results to other independent data sets such as: radar, OTD, LIS, Lightning Detection and Ranging (LDAR), and the NLDN. The first author will also improve some of the matrix methods presented here to directly account for Earth sphericity; more elegant oblate spheroidal models are also under consideration.

Acknowledgments. We appreciate the work of Susan Burrer in completing the final form of this manuscript, and the work of Janine Roskowski for her help in preparing the final figures. In addition, we are thankful to: Mike Stewart, David Slaton, Jim Core, Steven Rutledge, Steven Tirus, and other MCTEX personnel for their assistance in the deployment, testing, and maintenance of the ALDF sites that stimulated the theoretical work provided in this writing.

References

- Christian H. J., R. J. Blakeslee, and S. J. Goodman, *Lightning Imaging Sensor (LIS) for Earth Observing System*, NASA TM-4350, pp. 1-36, 1992.
- Cummins, K. L., R. O. Burnett, W. L. Hiscox, and A. E. Pifer, Line reliability and fault analysis using the National Lightning Detection Network, *Precise Measurements in Power Conference*, Arlington, VA, Oct. 27-29, 1993.
- Cummins, K. L., E. A. Bardo, W. L. Hiscox, R. B. Pyle, and A. E. Pifer, NLDN'95: A combined TOA/MDF technology upgrade of the U.S. National Lightning Detection Network, *International Aerospace & Ground Conference on Lightning and Static Electricity*, Williamsburg, VA, Sept. 26-28, 1995.
- Cummins, K. L., M. J. Murphy, E. A. Bardo, W. L. Hiscox, R. B. Pyle, and A. E. Pifer, A combined TOA/MDF technology upgrade of the U. S. National Lightning Detection Network, *J. Geophys. Res.*, 103, No. D8, pp. 9035-9044, 1998.
- Goodman, S. J., H. J. Christian, R. J. Blakeslee, W. J. Koshak, D. M. Mach, and W. L. Boeck, The Optical Transient Detector: First results, *Proceedings 1995 IUGG XXI Meeting*, Boulder, CO, July 2-14, 1995.
- Hiscox, W. L., E. P. Krider, A. E. Pifer, and M. A. Uman, A systematic method for identifying and correcting "site errors" in a network of magnetic direction finders, Preprints, *International Aerospace and Ground Conference on Lightning and Static Electricity*, Orlando, FL, National Interagency Coordination Group, July 1-5, 1984.
- Holle, R. L., and R. E. Lopez, Overview of real-time lightning detection systems and their meteorological uses, *NOAA Tech. Memo. ERL NSSL-102*, 1993.
- Keenan, T., G. Holland, S. Rutledge, J. Simpson, J. McBride, J. Wilson, M. Moncrief, R. Carbone, W. Frank, B. Sanderson, and J. Hallett, Science Plan Maritime Continent Thunderstorm Experiment (MCTEX), *BMRC Research Report 44*, Melbourne, Australia, 3001, 66 pp., 1994.

Copyright 1998 by the American Geophysical Union.

Paper number 98JA

Appendix A—Weighting of Bearing Data

It is of interest to determine to what extent bearing data is actually being used to constrain the lightning source location in the LP method as a function of the weighting factor δ introduced into the linear system of equations provided in (11). Insight is gained by considering the case of 3 sensors and ignoring field measurements, F_i . Then (11) reduces to

$$\begin{bmatrix} \alpha_2 \\ \alpha_3 \\ \delta\beta_1 \\ \delta\beta_2 \\ \delta\beta_3 \end{bmatrix} = \begin{bmatrix} (x_2 - x_1) & (y_2 - y_1) & c(t_1 - t_2) \\ (x_3 - x_1) & (y_3 - y_1) & c(t_1 - t_3) \\ \delta \sin \phi_1 & -\delta \cos \phi_1 & 0 \\ \delta \sin \phi_2 & -\delta \cos \phi_2 & 0 \\ \delta \sin \phi_3 & -\delta \cos \phi_3 & 0 \end{bmatrix} \begin{bmatrix} x \\ y \\ d_i \end{bmatrix}. \quad (\text{A-1})$$

This system, which can be written in the standard notation: $\mathbf{g} = \mathbf{K}\mathbf{f}$, has the least squares solution $\mathbf{f} = (\tilde{\mathbf{K}}\mathbf{K})^{-1}\tilde{\mathbf{K}}\mathbf{g}$. We are interested in the explicit functional dependence of x and y on the arrival time, t_i , and bearing, ϕ_i , data, and on the weighting factor, δ . Because this is a very involved hand calculation, we utilize a computer-aided symbolic manipulator to arrive at the following form

$$x = \frac{1}{h_0\delta^2 + h_1} \left[h_2\alpha_2 + h_3\alpha_3 + \sum_{j=4}^6 (h_j\delta^2 + h_{j+3})\beta_{j-3} \right]. \quad (\text{A-2})$$

The ten functions, h_j ($j = 0, \dots, 9$) depend, in general, on the arrival time and bearing data. The variables (α_2, α_3) depend only on arrival time data and network geometry, and the variables $(\beta_1, \beta_2, \beta_3)$ depend only on bearing data and network geometry as given in (3) and (6), respectively. A similar form holds for y . The coefficient in front of the square brackets in (A-2) does not preferentially weight the α 's or β 's so it is of no concern in this discussion. However, the

coefficients $(h_j + \delta^2 h_{j+3})$ do weight the β 's but not the α 's (i.e., these coefficients weight the bearing data, but not the arrival time data). This leads to the final results

$$\delta = 0 \Rightarrow \text{no solution}$$

$$\lim_{\delta \rightarrow \infty} x = \frac{1}{h_0} (h_4 \beta_1 + h_5 \beta_2 + h_6 \beta_3) \equiv \Lambda(\phi_i); \quad i = 1, 2, 3. \quad (\text{A-3})$$

The first result is true since when $\delta = 0$ there are 2 equations in three unknowns in (A-1). The second result is true because the only arrival time dependence associated with each function (h_0, h_4, h_5, h_6) is a factor $(t_2^2 + t_3^2)$. When the ratios h_j/h_0 are taken this factor cancels out and we are left with a function, Λ , that depends only on bearing data.

In summary, for a positive finite value of δ , both arrival time and bearing data are utilized. However, as δ is increased from zero, bearing data eventually becomes more heavily weighted over arrival time data until, for a sufficiently large value of δ , only bearing data is being used to determine the source location. For $\delta = 1$, we have difficulty inverting \mathbf{K} for many source locations. We have also performed retrievals, in the presence of measurement errors, for the values: $\delta = 10, 10^2, 10^3, 10^4, 10^5$, and 10^6 . Figure A.1 shows the result for $\delta = 10, 10^3$, and 10^5 . There is not much change in the solution from 10 to 10^3 , but the dominance of bearing data constraints at 10^5 begins to reduce the quality of the solution (i.e., a 2° random bearing error can create a substantial location error if the source range is sufficiently large).

We have performed the same type of computer-aided symbolic manipulation to determine explicit forms when a four sensor network is used (i.e., one more arrival time equation and one

more bearing equation is added to the system in A-1 so that \mathbf{K} becomes a 7x3 matrix). In this case, the form of x (as well as y) is

$$x = \frac{1}{k_0\delta^4 + k_1\delta^2 + k_2} \left[\sum_{j=2}^4 (k_{j+1}\delta^2 + k_{j+4})\alpha_j + \sum_{j=1}^4 (k_{j+8}\delta^4 + k_{j+12}\delta^2)\beta_j \right]. \quad (\text{A-4})$$

Most of the 17 functions, k_j , $j = 0, \dots, 16$ depend on both arrival time and bearing data. However, (k_2, k_6, k_7, k_8) depend on arrival time data, but do not depend on bearing data. We obtain the final limiting conditions

$$\begin{aligned} \lim_{\delta \rightarrow 0} x &= \frac{1}{k_2} (k_6\alpha_2 + k_7\alpha_3 + k_8\alpha_4) \equiv \Gamma(t_i) \\ \lim_{\delta \rightarrow \infty} x &= \frac{1}{k_0} (k_9\beta_1 + k_{10}\beta_2 + k_{11}\beta_3 + k_{12}\beta_4) \equiv \Omega(\phi_i); \quad i = 1, 2, 3. \end{aligned} \quad (\text{A-5})$$

Hence, we swing from a solution governed only by timing data ($\delta = 0$) to one governed only by bearing data ($\delta = \infty$). The solutions for $\delta = 10$, 10^3 , and 10^5 are shown in Figure A.2. The bearing data significantly worsens the solution when weighted heavily ($\delta = 10^5$).

Appendix B—Locations Where QP Method Discriminant Function Vanishes

We investigate more rigorously the zeroes of the discriminant function $\Delta \equiv (B^2 - 4AC)$ of (27) in the QP method. The computer plots of this function gave some interesting results near the outer baselines of the sensors, i.e., there appears to be minima there (see Fig. 11).

In the following formal approach, we algebraically reduce the discriminant into the product of three factors. Each factor is then shown to vanish along a specific outer sensor baseline. Our results apply to arbitrary network geometries. Because a zero discriminant implies that two nonnegative, real, and *equal* roots are obtained, a unique (unambiguous) solution $(x(r), y(r), t(r))$ is obtained on the outer sensor baselines where $r = -B/(2A) = r_+ = r_-$.

Using the forms in (26) for A , B , and C , the discriminant can be written as

$$\Delta = 4c^2 \left[(p^2 - r_2^2 r_3^2) (q_2'^2 t_3^2 - 2q_2' q_3' t_2 t_3 + q_3'^2 t_2^2) + \varepsilon^2 \sigma \right], \quad (\text{B-1})$$

where

$$\begin{aligned} p &= \mathbf{r}_2 \cdot \mathbf{r}_3 = x_2 x_3 + y_2 y_3 \\ \varepsilon &= \frac{1}{c} \det \mathbf{Q} = \frac{1}{c} (x_2 y_3 - y_2 x_3) \\ \sigma &= r_3^2 q_2'^2 - 2p q_2' q_3' + r_2^2 q_3'^2. \end{aligned} \quad (\text{B-2})$$

To simplify some of the algebra without losing generality, we rotate the x and y axes so that $y_2 \equiv 0$. Further reduction of (B-1) leads to

$$\Delta = \left[x_2^2 y_3^2 (x_2^2 - c^2 t_2^2) \right] \left[r_3^2 - c^2 t_3^2 \right] \left[(x_2^2 - c^2 t_2^2) + 2(c^2 t_2 t_3 - x_2 x_3) + (r_3^2 - c^2 t_3^2) \right]. \quad (\text{B-3})$$

Figure B.1 considers the second factor, $(r_3^2 - c^2 t_3^2)$, in (B-3). For a source located on the solid line with $r \geq r_3$ site three is excited at

$$t_3 = t + \frac{r - r_3}{c} = \frac{-r}{c} + \frac{r - r_3}{c} = -\frac{r_3}{c} . \quad (\text{B-4})$$

The factor becomes

$$(r_3^2 - c^2 t_3^2) = r_3^2 - c^2 \left(-\frac{r_3}{c} \right)^2 = r_3^2 - r_3^2 = 0 . \quad (\text{B-5})$$

Proceeding in a similar fashion, the factor for a source on the dashed line with $0 < r < r_3$ is the nonzero result, $4r(r_3 - r)$, and the factor for a source on the dotted line (with $0 \leq r < r_3$) or a source on the thick line (with $r \geq r_3$) is zero. Hence, the factor is zero along the line running through the sensors (including the sensor locations themselves, but excluding the line segment between the sensors). This is what we refer to as the “outer sensor baselines”. Similar comments can be made regarding sites 1 and 2 when the factor $(x_2^2 - c^2 t_2^2)$ is considered.

Evidently the third factor in (B-3) corresponds to the line running through sites 2 and 3. To prove this, we consider the geometry provided in Figure B.2. For a source on the solid line with $d \geq 0$ we have

$$t_2 = \frac{D + d - r}{c} \quad (\text{B-6})$$

$$t_3 = \frac{d - r}{c} .$$

Substituting these expressions into the third factor, and noting that $D^2 = (x_2 - x_3)^2 + y_3^2 = x_2^2 - 2x_2x_3 + r_3^2$, we obtain

$$\begin{aligned}
 & x_2^2 - (D + d - r)^2 + r_3^2 - (d - r)^2 + 2(D + d - r)(d - r) - 2x_2x_3 \\
 &= (x_2^2 - 2x_2x_3 + r_3^2) - [(D + d - r) - (d - r)]^2 \\
 &= (x_2^2 - 2x_2x_3 + r_3^2) - D^2 = 0 .
 \end{aligned} \tag{B-7}$$

For a source located on the dashed line (but not at site 2 or site 3) the factor reduces to the nonzero result: $4\omega_2\omega_3[(x_2 - x_3)^2 + y_3^2]$, where the constant factors (ω_2, ω_3) obey the constraints: $\omega_2 + \omega_3 = 1$, $\omega_2 > 0$, $\omega_3 > 0$. Finally, for a source on the dotted line and a distance $l \geq 0$ from site 2, we have

$$\begin{aligned}
 t_2 &= \frac{l - r}{c} \\
 t_3 &= \frac{D + l - r}{c} .
 \end{aligned} \tag{B-8}$$

These expressions have the same form as those in (B-6) but are interchanged. When substituted into the third factor of (B-3), the factor reduces to zero as in (B-7). This completes the proof showing that the discriminant function vanishes along the outer sensor baselines.

Figure 1. Geometry associated with the LP method.

Figure 2. Spherical trigonometry used for determining arrival time and bearing.

Figure 3. Lightning location retrieval errors for a three-station network using the LP method: (a) no measurement errors, and (b) with the following random measurement errors: 0.5-m sensor location error, 300-ns timing error, 2° bearing error. Mapping #1 is used. Contours are in units of kilometers. The analysis region shown is 6° in latitude (667 km) by 6° in longitude (about 651 km), and this is where the Maritime Continent Thunderstorm EXperiment (MCTEX) was conducted.

Figure 4. Same as in Figure 3 except that Mapping #2 is used.

Figure 5. Same as in Figure 3 except that four sensors are used.

Figure 6. Same as in Figure 3 except that four sensors and Mapping #2 are used.

Figure 7. Same as in Figure 3 except that this is for the Tropical Ocean Global Atmosphere Coupled Ocean-Atmosphere Response Experiment (TOGA-COARE) analysis region, and mapping #2 is used. The analysis region is 18° in latitude (2002 km) by 18° in longitude (about 1996 km). Shading, rather than contouring, is used to clarify the non-monotonic distribution of retrieval errors.

Figure 8. Comparison of roots in the QP method. The shaded regions indicate where root r_+ produces better retrieval results than root r_- . The unshaded regions indicate where root r_- produces better retrieval results than root r_+ . No measurement errors have been added to the simulated data.

Figure 9. Retrieval errors from the optimum root in the QP method: (a) no measurement errors, and (b) with the following random measurement errors: 0.5-m sensor location error, 300-ns timing error. Mapping #1 is used. Contours are in units of kilometers.

Figure 10. Shaded regions are the QP method “ambiguity regions” that indicate what lightning source locations result in two unequal nonnegative real roots. No errors were added to the simulated arrival times.

Figure 11. Plot of the (scaled) discriminant of the QP method. Expressions for A , B , and C in the discriminant, $B^2 - 4AC$, are given in (26) of the manuscript.

Figure 12. Fraction of 100 simulated sources at each location that produce complex roots using the QP method. A 0.5-m sensor location error, a 300-ns timing error, and Mapping #1 was used.

Figure A.1 Location retrieval errors for a three station network using the LP method when (a) $\delta = 10$ (b) $\delta = 10^3$ and (c) $\delta = 10^5$. The same simulated measurement errors discussed in section 3 are used: 0.5-m sensor location error, 300-ns timing error, 2° bearing error. Mapping #2 is used. The contours are in units of kilometers.

Figure A.2 Same as in Figure A.1, but for a four station network.

Figure B.1. Geometry for analyzing the second factor in the discriminant function.

Figure B.2. Geometry for analyzing the third factor in the discriminant function.

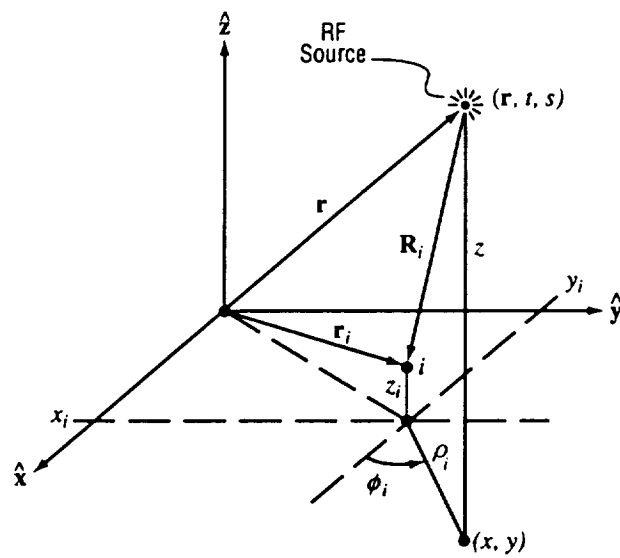


Fig.1
5-31469

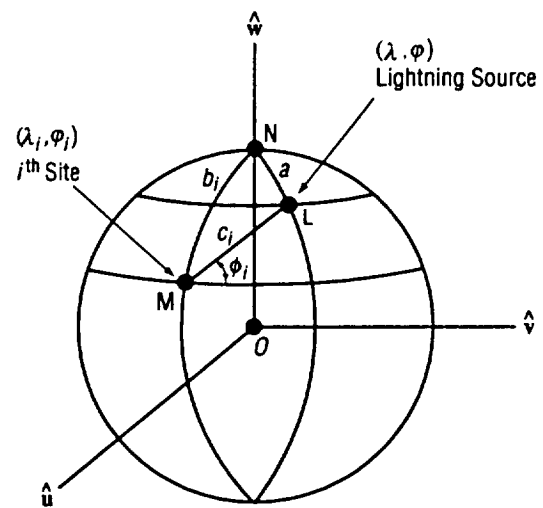


Fig. 2
5-31470

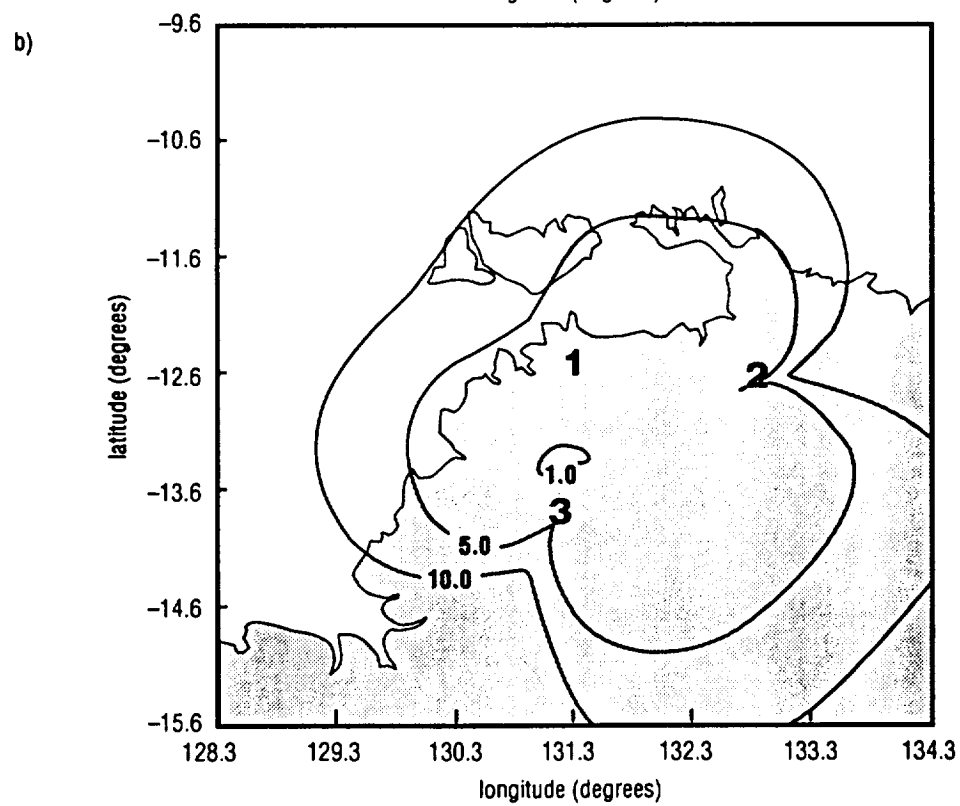
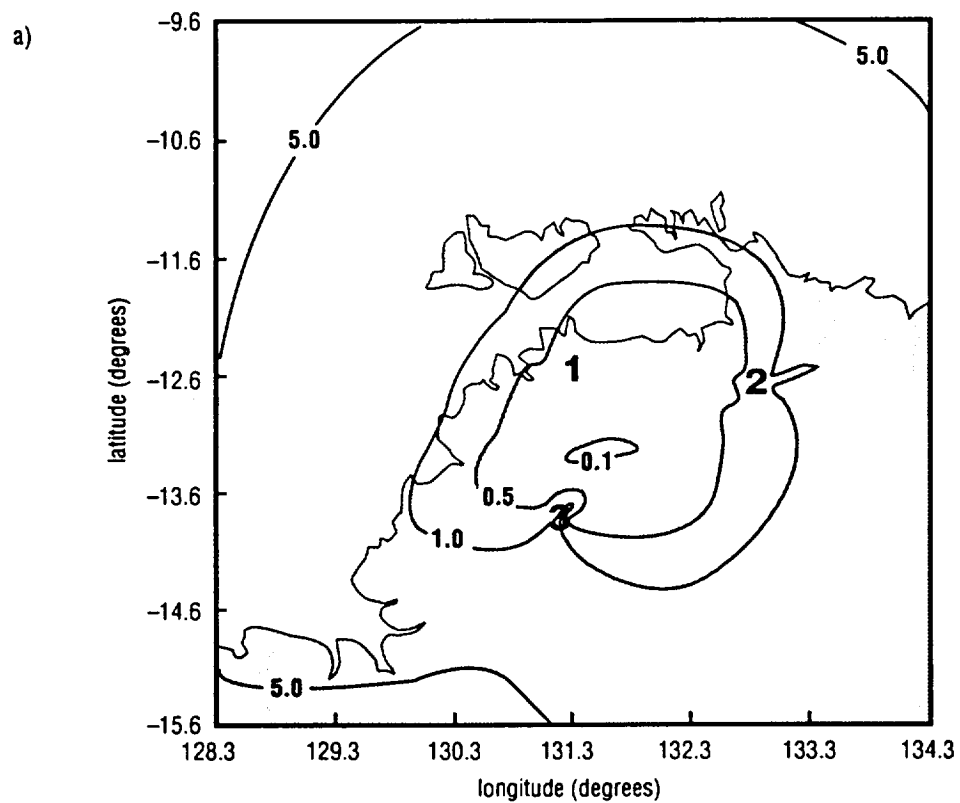


Fig. 3
5-31471

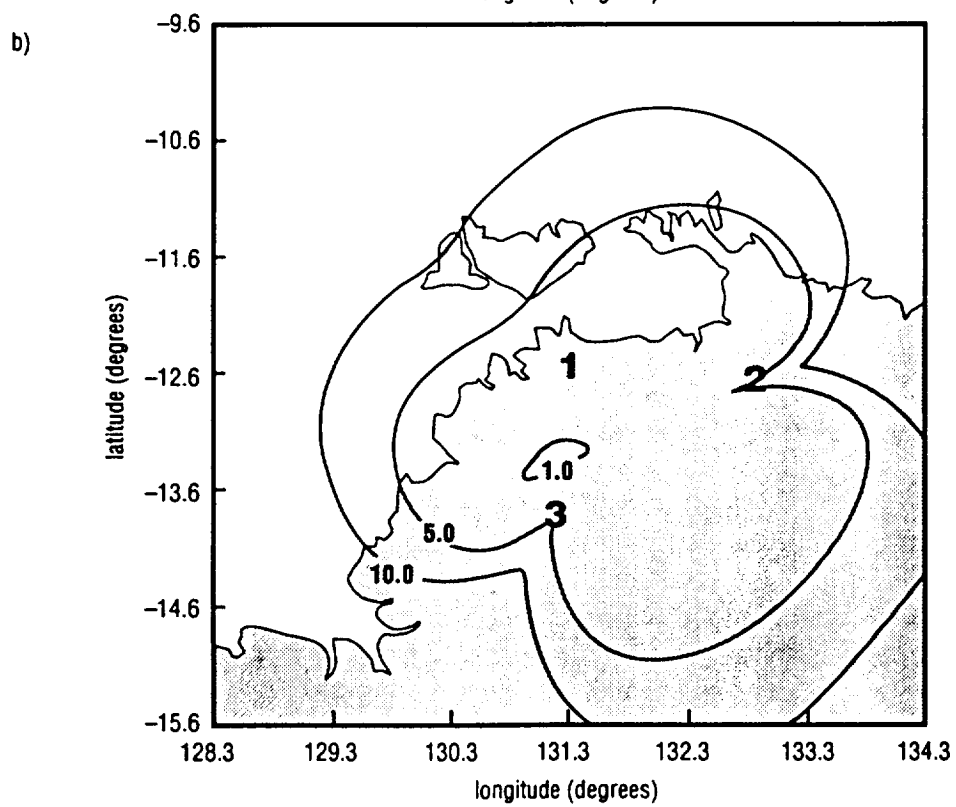
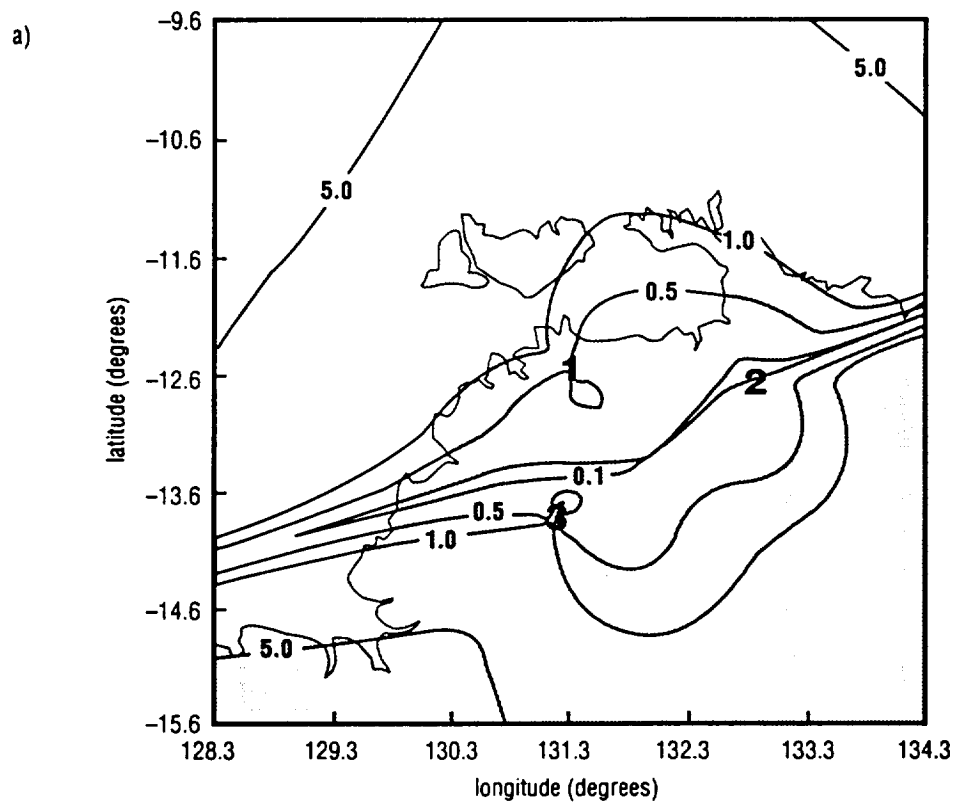


Fig.4
5-31473

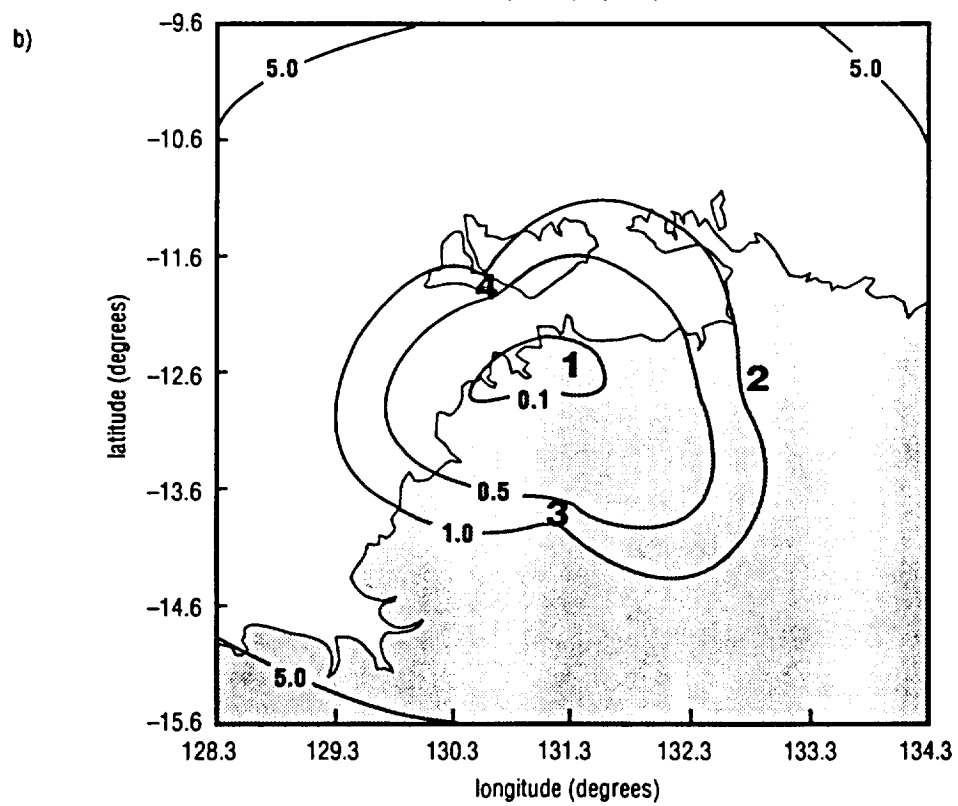
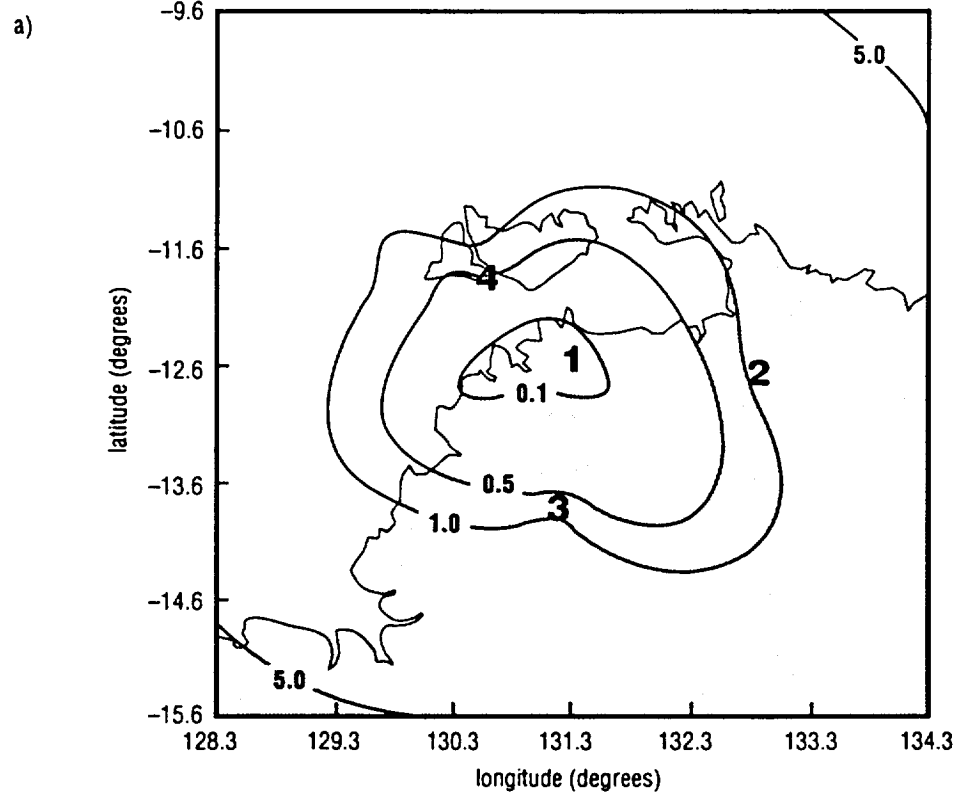


Fig.5
5-31475

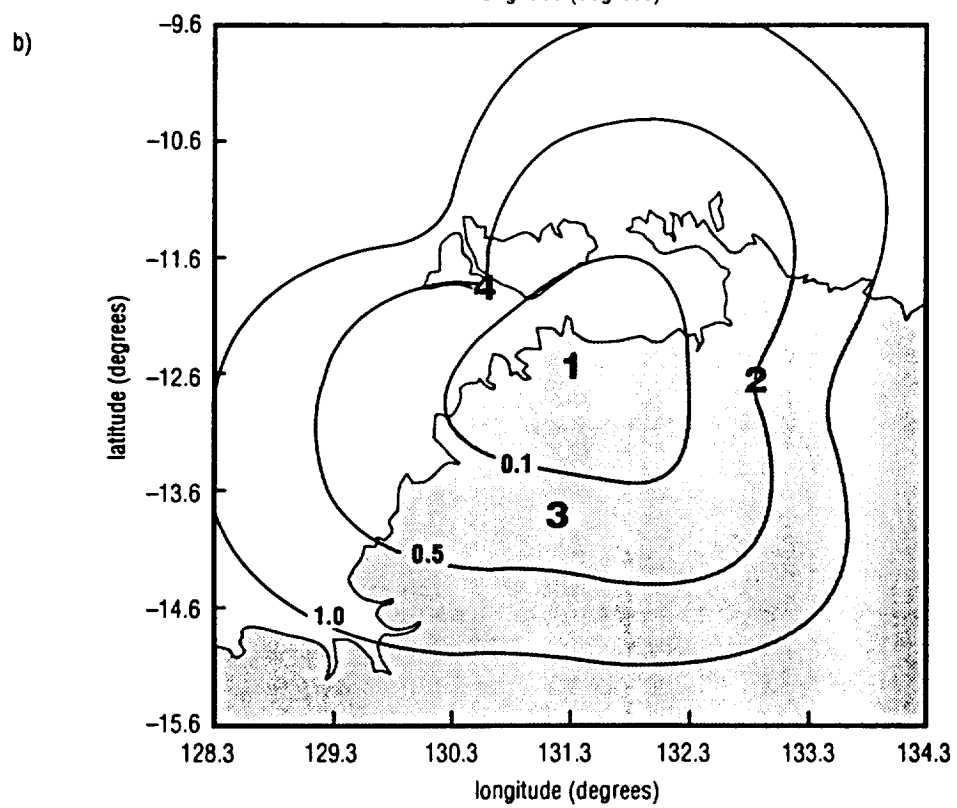
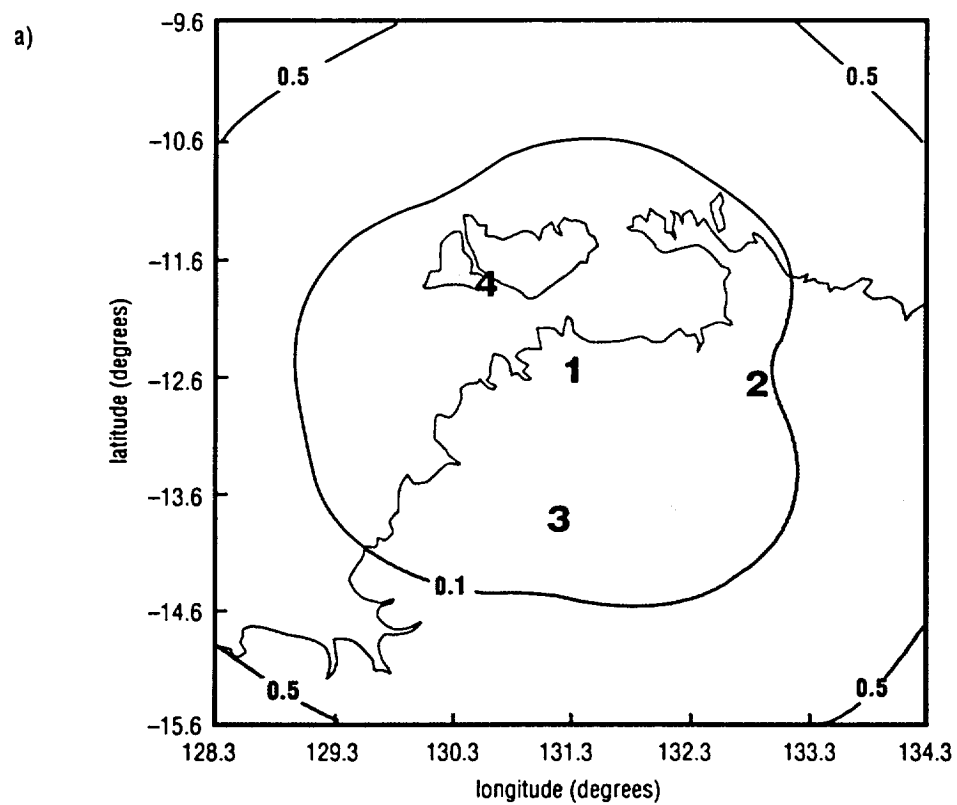
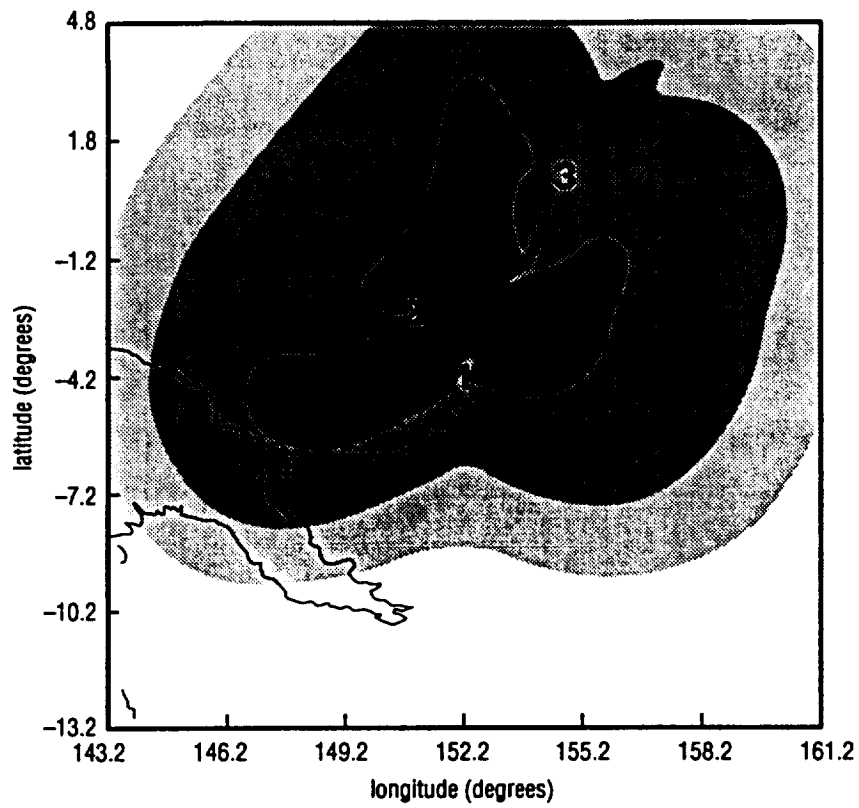
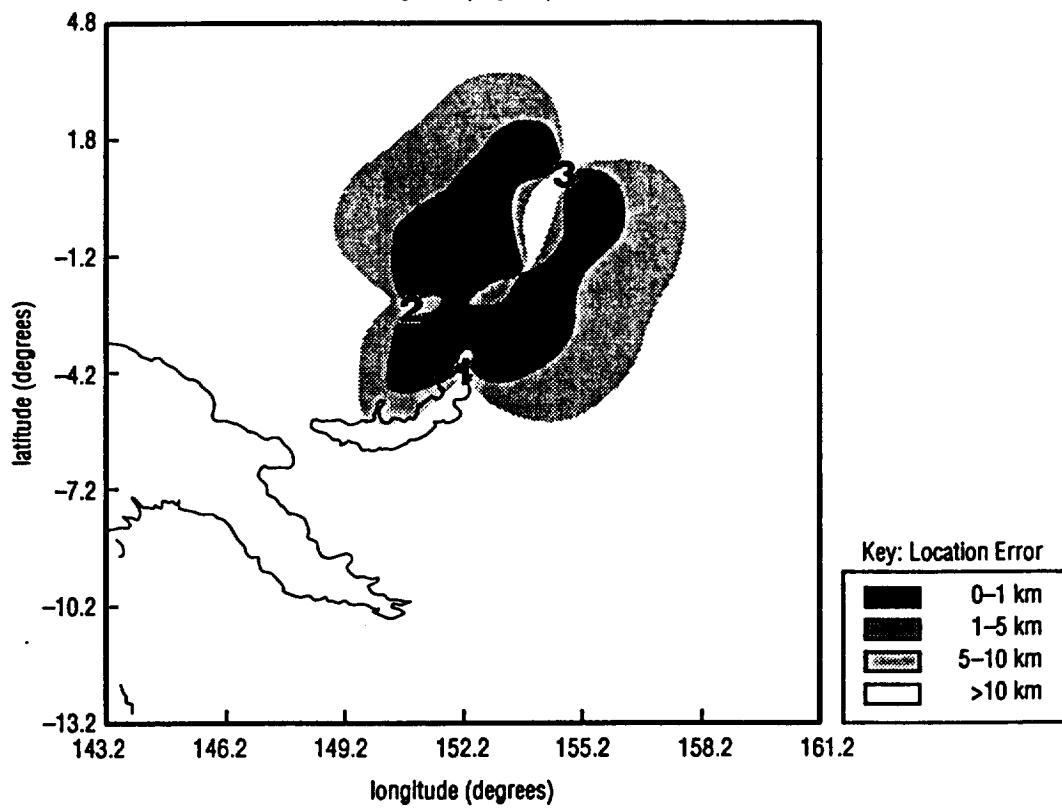


Fig. 6
5-31477

a)



b)



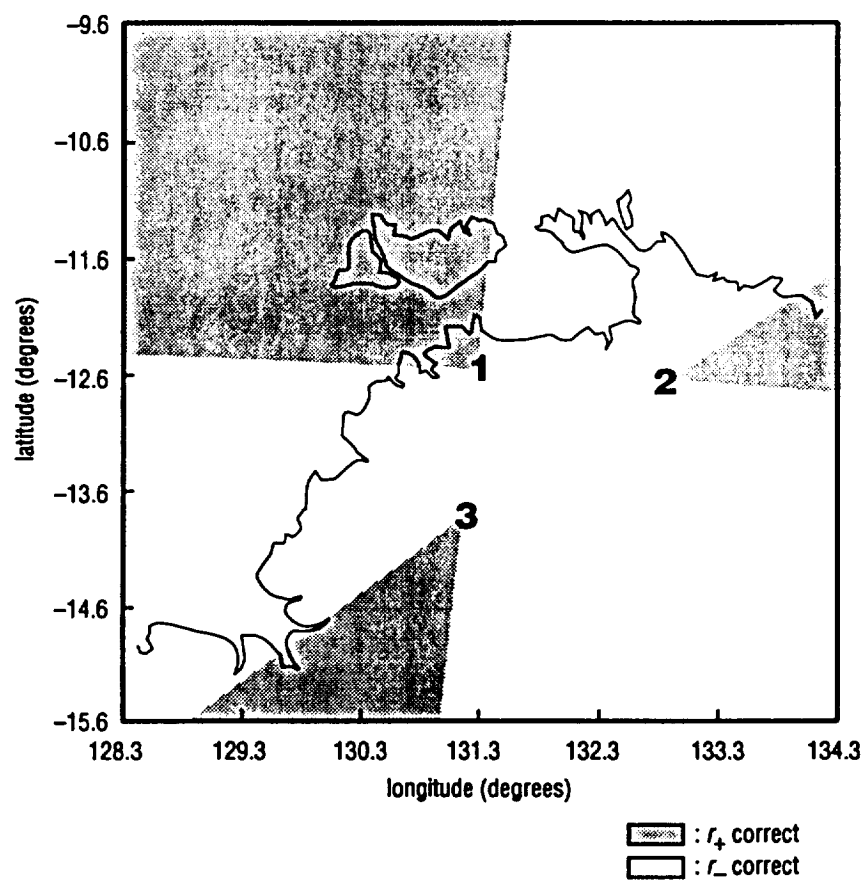


Fig.8
5-31483

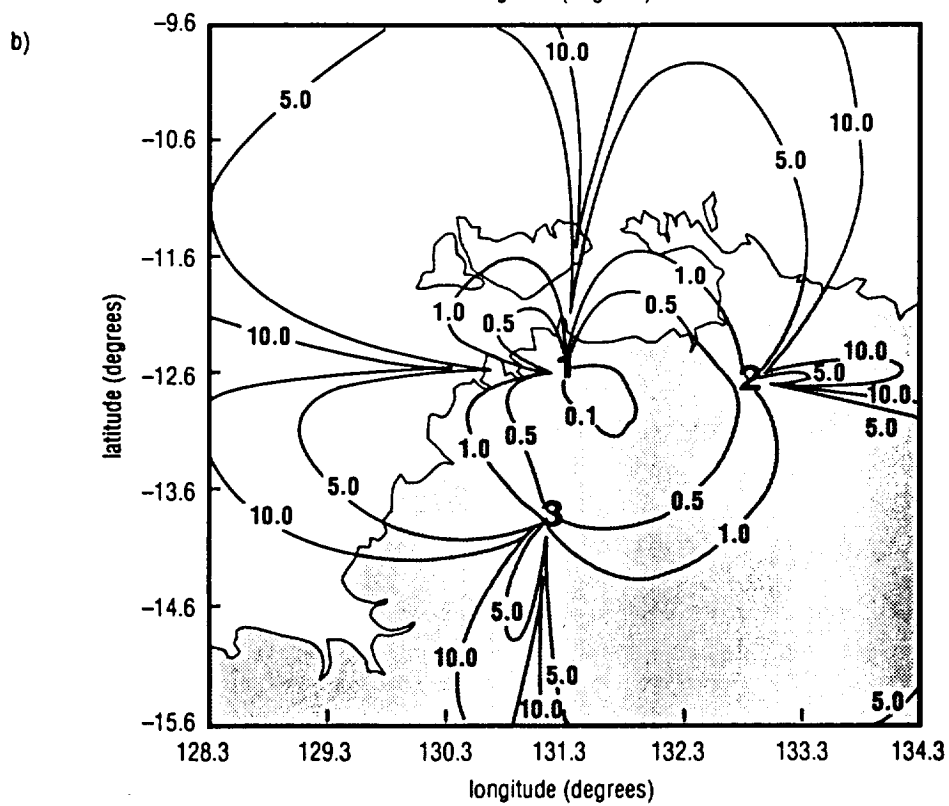
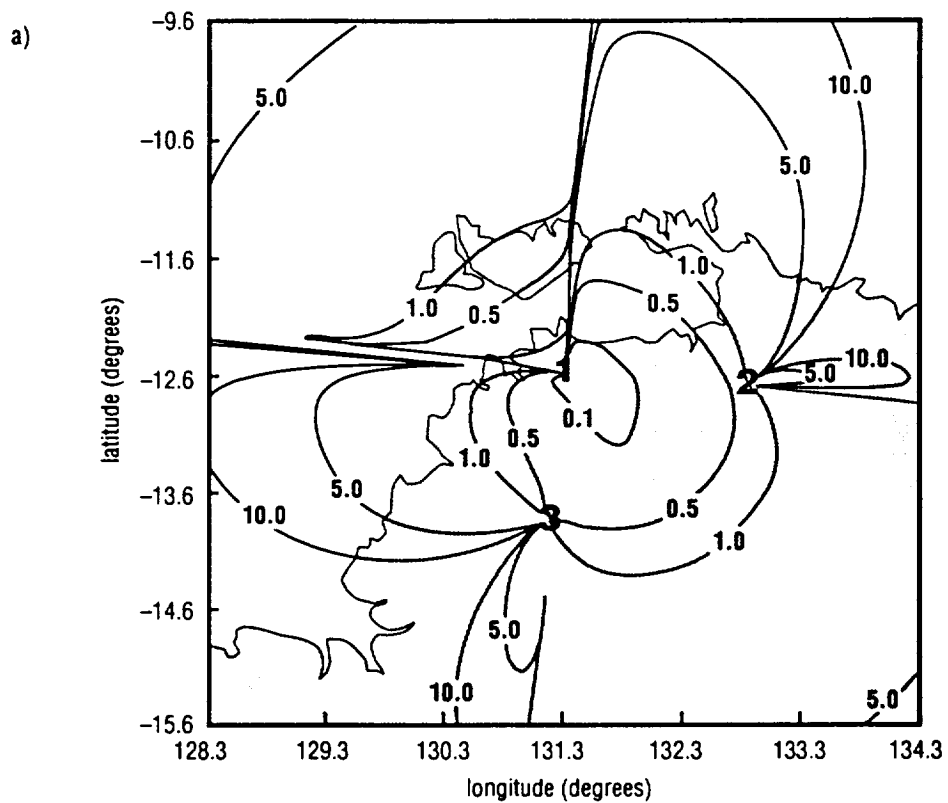


Fig.9
5-31484

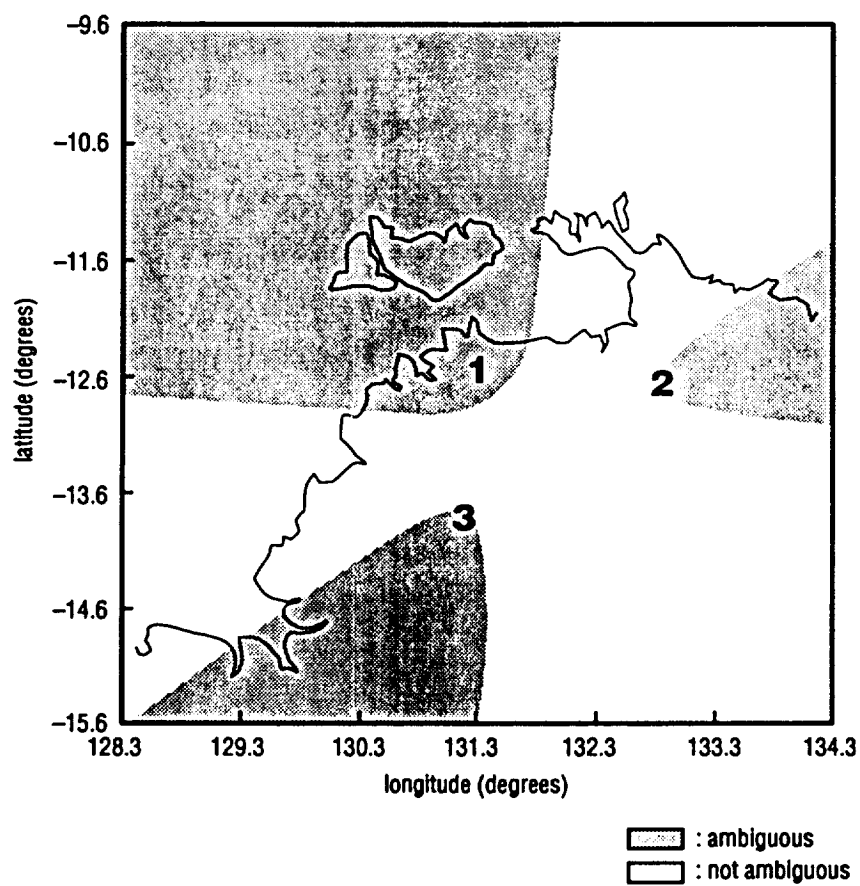


Fig.10
5-31486

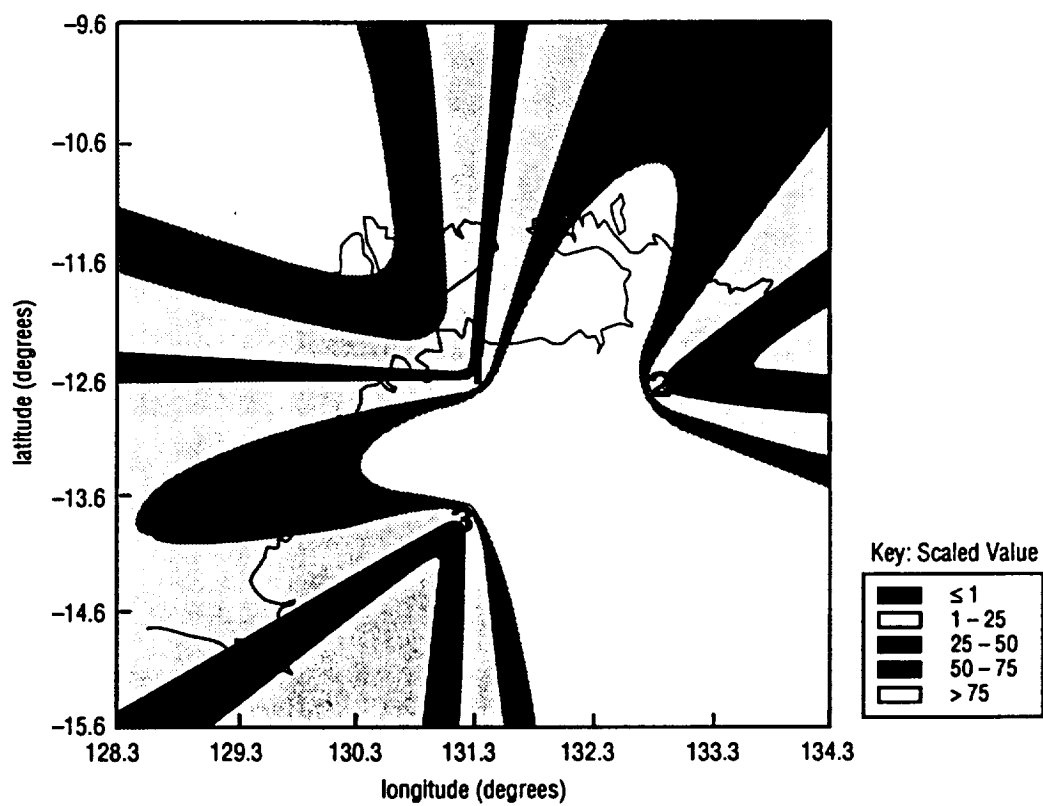


Fig.11
5-31487

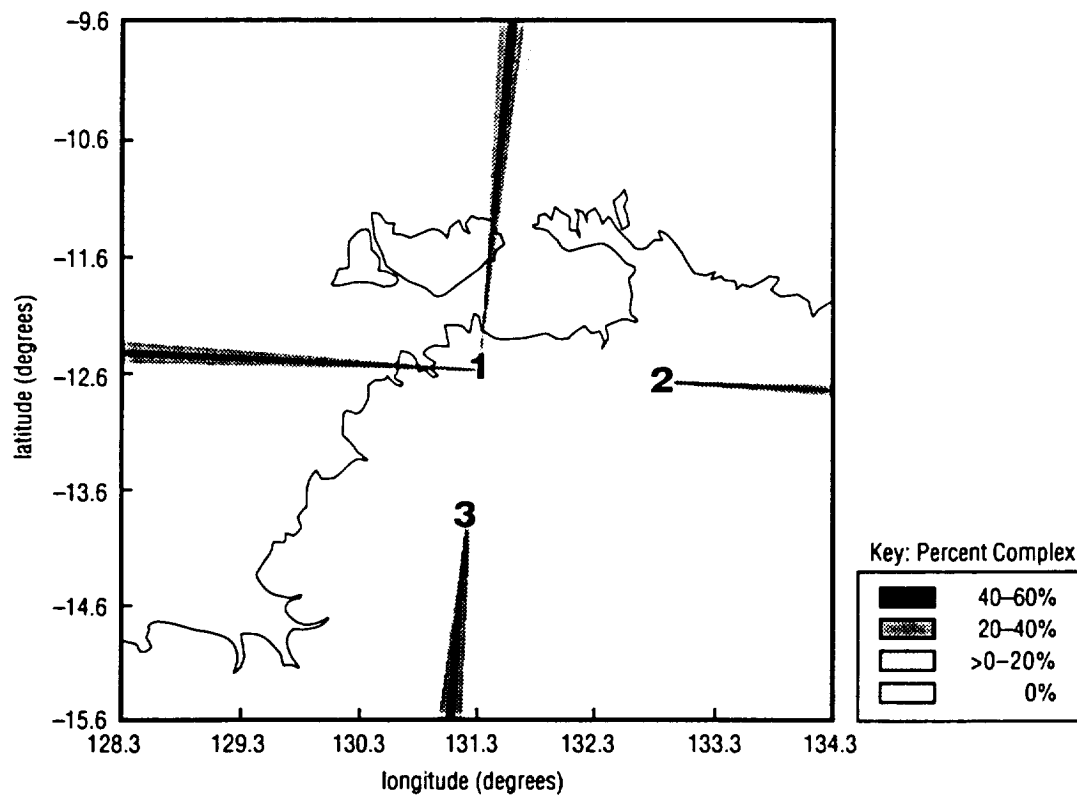


Fig.12
5-31605

